Check for updates

Cite this: *RSC Adv.*, 2022, **12**, 14377

Investigations on the thermoelectric and thermodynamic properties of Y$_2$CT$_2$ (T = O, F, OH)

Li Wang,† Wen-Li Chang, ●†* Zi-Qi Sun and Zi-Meng Zhang

Using the first-principle calculations combined with the Boltzmann transport theory, we studied the thermoelectric properties of Y$_2$CT$_2$ (T = O, F, OH) MXenes. Specifically, the Seebeck coefficient, thermal and electrical conductivities under constant relaxation time approximation were calculated. Results show that for p-type carriers, Y$_2$CO$_2$ has the largest power factor of up to 0.0017 W m^{-1} K^{-2} when the carrier concentration is 4.067 × 10^{13} cm^{-2} at 900 K, at the same temperature, for n-type carriers, the concentration is 9.376 × 10^{13} cm^{-2}, the power factor in Y$_2$C(OH)$_2$ is 0.0026 W m^{-1} K^{-2}. In particular, the figure of merit in Y$_2$CF$_2$ is 1.38 at 900 K because of its low thermal conductivity, indicating that it can be considered a potential medium-temperature thermoelectric material. In addition, the thermodynamics properties within 32 GPa and 900 K, such as bulk modulus, heat capacity and thermal expansion, are also estimated using the quasi-harmonic Debye model. Our results may offer some valuable hints for the potential application of Y$_2$CT$_2$ (T = O, F, OH) in the thermoelectric field.

1 Introduction

Due to the increase in energy consumption and severe environmental problems, it is of great significance to explore sustainable and ecologically sound energy resources. Thermoelectric materials (TE) can realize the conversion directly between heat and electricity.[1] This unique feature makes the expectation from thermoelectric materials deal with the global energy crisis.[2] The performance of thermoelectric materials is evaluated by the dimensionless quality factor *ZT*, which is defined as, $ZT = \frac{S^2\sigma}{\kappa} T^3$ where *S* is the Seebeck coefficient, σ is the electrical conductivity, κ is the sum of electronic thermal conductivity κ_e and the lattice thermal conductivity κ_l, and *T* is the temperature.[4,5] The thermopower is evaluated by the power factor $S^2\sigma$.[6,7] Generally, both, high $S^2\sigma$ and low κ lead to secure high *ZT* value.[8,9] In the past few decades, a series of high-efficiency thermoelectric materials have been discovered.[10] Among them, the typical thermoelectric materials with *ZT* > 1 have Bi$_2$Te$_3$, Si$_{1-x}$Ge$_x$, and PbTe.[11] Unfortunately, the Carnot efficiency of thermoelectric materials is only 10% in practical applications, which has a great difference from traditional refrigeration with a Carnot efficiency of 30%.[12] Although scientists have developed many methods to improve the performance of thermoelectric materials, they, however, still face many challenges; *ZT* is difficult to increase due to the coupling between thermoelectric factors.

Nanostructuring is one of the effective ways to improve *ZT*.[13,14] In 1993, Hicks and Dresselhaus expected that the quantum confinement effect of electronic carriers in low-dimensional materials can significantly improve the power factor,[14] and they found that there is a *ZT* value of up to 2.62 at 923 K[15] in a two-dimensional SnSe single crystal, indicating it may be possible that they may be promising thermoelectric materials.[16] MXenes is a new type of two-dimensional material, which has been extensively studied for its potential applications in the fields of energy storage and conversion, environment and catalysis, separation membranes, medicine, optics and electronics.[17] MXenes are formed by etching the A element from the MAX phase in an aqueous hydrofluoric acid solution.[18] MAX phases with the chemical formula M$_{n+1}$AX$_n$ (*n* = 1, 2 or 3) have a layered structure, where M is an early transition metal, A is a group of elements, and X is nitrogen or carbon.[19] During the etching process, A atoms are usually replaced by O, F and/or OH groups, resulting in functionalized MXenes M$_{n+1}$X$_n$T$_2$.[20] Research on the thermoelectric properties of MXene materials mainly focuses on MXenes with semiconductor properties, such as Sc$_2$CT$_2$ (T = O, F, OH)[21] and M$_2$CO$_2$ (M = Ti, Zr, Hf),[22] and surface functionalization can convert the metal abundance of MXenes into semiconductor properties,[23] and research shows that surface-functionalized Y$_2$C has semiconductor properties;[24] thus, in this work, we mainly studied the electronic structure and thermoelectric properties of the surface-functionalized Y$_2$C.

2 Calculation details

All calculations are performed based on the first principles. We firstly performed the structural optimization of Y$_2$CT$_2$ (T = O, F,

The School of Mathematics and Physics, Lanzhou Jiaotong University, 88 Anning West Road, Anning District, Lanzhou Cit 730070, China. E-mail: wlchang@mail.lzjtu.cn; Tel: +86-0931-4956005

† These authors contributed equally to this work.

OH) by using Vienna *Ab initio* Simulation Package (VASP).[25,26] The exchange-correlation functionals were treated by the generalized gradient approximation (GGA) with Perdew–Burke–Ernzerhof (PBE).[27] The energy cutoff 500 eV and the Monkhorst–Pack k-mesh $14 \times 14 \times 1$ were adopted. The thresholds of 0.005 eV Å^{-1} for the force convergence and 10^{-6} eV for the energy convergence were used. After relaxing the geometry structure, we calculated the band structure for Y_2CT_2 (T = O, F, OH) from the WIEN2k code, a full-potential linearized augmented plane-wave method.[28] The value of energy cutoff $R_{MT} \times K_{max}$ was taken to be 7, where R_{MT} is the smallest atomic sphere radius in the unit cell of Y_2CT_2 (T = O, F, OH), and K_{max} is the magnitude of the largest K vector. More-dense k-point mesh of $15 \times 15 \times 1$ was adopted in order to ensure the convergence of the electronic transport properties.

We solved the semi-classical Boltzmann transport equation within the constant relaxation time approximation ($\tau = 10^{-14}$ s)[29] for calculating the Seebeck coefficient, electrical conductivity, and thermal conductivity. While the relaxation time τ generally depends on the electronic wave vector, energy, and scattering mechanism, reliable results for the transport properties have been obtained within the constant relaxation time approximation for a variety of materials.[30–32] A rigid band model was used to simulate doping by shifting the chemical potential (BoltzTraP code).[33] For this purpose, the electronic band structure was calculated on a very fine $60 \times 60 \times 1$ k-mesh.

3   Results and discussion

3.1   Electronic properties

First, we built the structural model Y_2CT_2 (T = O, F, OH) as shown in Fig. 1, the three-dimensional periodic boundary conditions were combined with the 20 Å thick vacuum region along the c direction to produce a single layer structure, and optimize their structure to obtain the ground state. The lattice parameters at equilibrium are presented in Table 1. It was found that the O and OH functionalization leads to longer Y–C in Y_2CO_2 and Y–T in $Y_2C(OH)_2$ respectively, this difference is also reflected in the smaller bond angle of $\angle CYC$ in Y_2CO_2 and $\angle TYT$ in $Y_2C(OH)_2$, because the proximity of O and OH to C leads to the redistribution of charges, which weakens the bond strength of Y–C in Y_2CO_2 and Y–T in $Y_2C(OH)_2$.

Since their structures are the same, the three functionalized Y_2C studied here have similar energy band structures, as shown in Fig. 2. According to Fig. 2, an indirect band gap in Y_2CO_2 and Y_2CF_2 was observed, the maximum valence band is at the Γ point, and the minimum conduction band was at the M point. In $Y_2C(OH)_2$, a direct band gap was found, and the maximum valence band and the minimum conduction band were both at Γ point. For O, F and OH functionalization, the band gap decreases sequentially. In addition, each compound exhibits asymmetry between the valence band and the conduction band, so the effective masses of p-type and n-type carriers are different. For the three compounds, Y-d, the C-p and T-s states form the valence band edge and the conduction band edge, among them, C-p contributes the most to the valence band
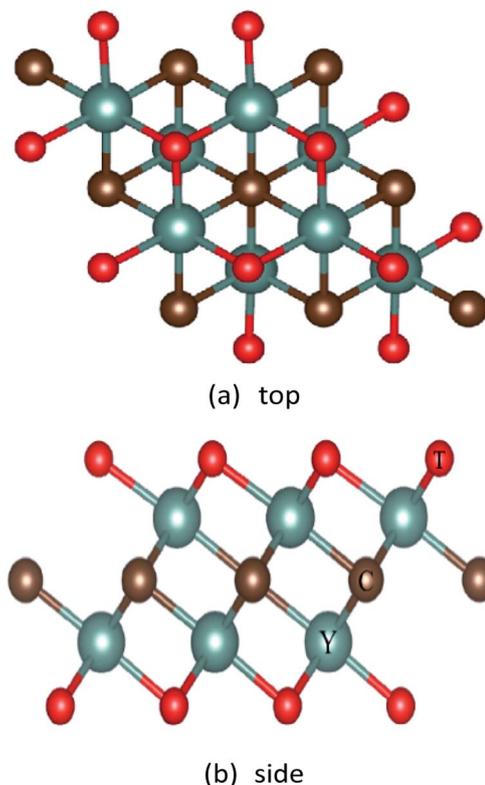

Fig. 1   Top and side views of the Y_2CT_2 (T = O, F and OH).

Table 1   Calculated lattice constants (Å), bond length (Å), bond angle and band gap (eV)

	a	Y–C	C–T	Y–T	$\angle$TYT	$\angle$CYC	Band gap
Y_2CO_2	3.54	2.70	3.25	2.18	108.81	81.76	3.63
Y_2CF_2	3.58	2.48	3.28	2.18	108.80	92.38	1.17
$Y_2C(OH)_2$	3.60	2.49	3.39	2.45	94.38	92.34	0.74

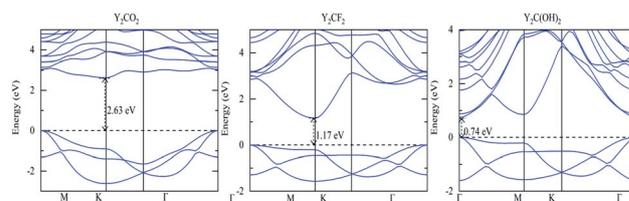**Fig. 2**   Electronic band structures of Y_2CT_2 (T = O, F and OH).

edge, and Y-d contributes the most to the conduction band edge, as shown in Fig. 3.

3.2   Thermoelectric properties

Flat bands near the Fermi level are beneficial to the thermoelectric properties of the material because they lead to higher S[34], that is, the greater the effective mass of the carrier, the greater is the S. The conduction band near the Fermi level of Y_2CO_2 is flatter than the valence band, which can be seen in Fig. 2. Therefore, for Y_2CO_2, the effective mass of n-type carriers
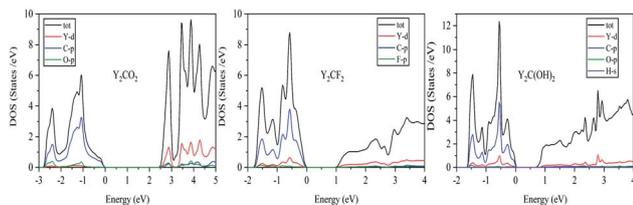
Fig. 3 Total and orbital densities of states of Y_2CT_2 (T = O, F and OH).

is greater than that of p-type carriers, while Y_2CF_2 and $Y_2C(OH)_2$ have opposite phenomena. As shown in Fig. 2 and Table 2. It can be observed from Fig. 4(a)–(f) that S for Y_2CO_2 n-type carriers is larger than S for p-type carriers, while Y_2CF_2 and $Y_2C(OH)_2$ are opposite. For all compounds, S increases with. Temperature and decreases with carrier concentration, which is consistent with Pisarenko's relationship[35]

$$S = \frac{8\pi^2 k_B^2}{3eh^2} m^* T \left(\frac{\pi}{3\rho} \right)^{\frac{2}{3}} \tag{1}$$

where m^* and ρ are the effective mass and carrier concentration, respectively. However, for the Y_2CF_2 and $Y_2C(OH)_2$, although high temperature should be beneficial to S, due to bipolar conduction (a large number of minority carriers), the carrier concentration will decrease as the temperature rises, and the smaller the band gap, the greater this effect, this is consistent with the reported results in ref. 20.

As expected, σ increases with ρ within a given temperature (300–900 K) and concentration (10^{10} to 10^{14} cm^{-2}), as shown in Fig. 5(a)–(f). Obviously, for Y_2CF_2 and $Y_2C(OH)_2$, the

Table 2 Effective mass m* (m_e) for p and n-types Y_2CT_2 (T = O, F and OH)

	Y_2CO_2	Y_2CF_2	$Y_2C(OH)_2$
p-type	1.19	2.53	2.17
n-type	1.79	0.57	1.21

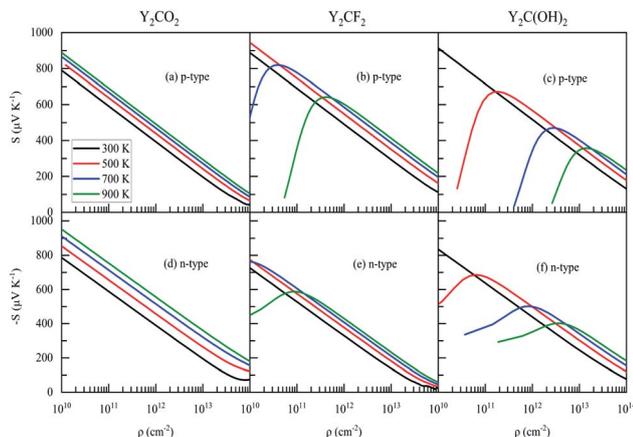**Fig. 4** Carrier concentration dependence of Seebeck coefficients (S) for (a)–(c) p-type and (d)–(f) n-type Y_2CT_2 (T = O, F and OH).

conductivity of n-type carriers is greater than that of p-type carriers because n-type carriers are superior to p-type carriers due to the dispersive conduction band near the Fermi-level conductivity. For all compounds, the conductivity decreased with increasing temperature. The change of κ_e is the same as that of σ, (see Fig. 5(g)–(l)). The difference is that κ_e increases with temperature. It can be clearly seen that for the three substances, the electronic thermal conductivity increases exponentially, this trend indicates that they have better thermal conductivity and can be used for heat dissipation in electronic devices. According to Fig. 6(a)–(f), the $S^2\sigma$ of the three compounds show similar trends. The $S^2\sigma$ value increased with increasing temperature. For the $S^2\sigma$ of Y_2CO_2 and Y_2CF_2 p-type carriers, the value is always greater than the $S^2\sigma$ value of the n-type carrier in a given carrier concentration (10^{10} to 10^{14} cm^{-2}) and temperature (300–900 K), which is determined by the effective carrier mass and the degree of dispersion of the band at the Fermi level. For the Y_2CO_2, Y_2CF_2 and $Y_2C(OH)_2$, the maximum values of $S^2\sigma$ appear in the vicinity of 2.0×10^{13}, 8.0×10^{13}, and 6.6×10^{13}, respectively.

For the lattice thermal conduction, the most commonly used method is solving the Boltzmann transfer equation (BTE), which involves the calculation of phonon frequency, group velocity, and harmonic and non-harmonic interatomic force constants (IFCs).[36,37] In order to consider the three phonon scattering processes, which need to be used to calculate the third-order anharmonic IFCs. Deinze et al.[38] used density functional perturbation theory (DFPT) to obtain third-order IFCs to study the phonon linewidth. In recent years, this method has been successfully used to solve BTE and predict the lattice thermal conductivity of materials.[39–41] This method requires the calculation of the electronic structure of multiple large supercells, and each supercell has a different set of atomic displacements, so it requires a lot of computing resources. A variety of simple and low-cost calculation methods have been developed to calculate the lattice thermal conductivity of materials. Among these, the Slack[42] is one of the more effective methods. In this work, the lattice thermal conductivity was calculated using the method proposed by Slack using the Debye temperature and the Grüneisen parameter:

$$\kappa_l(\Theta_a) = \frac{0.849 \times 3\sqrt[3]{4}}{20\pi^3(1 - 0.514\gamma^{-1} + 0.228\gamma^{-2})} \times \left(\frac{k_B\Theta_a}{\hbar} \right)^2 \frac{k_B m_a V^{\frac{1}{3}}}{\hbar\gamma^2} \tag{2}$$

where V is the volume of the unit cell, m_a is the average atomic mass and, γ is the Grüneisen parameter. Θ_a is the acoustic-mode Debye temperature,[42] which is different from the traditional Debye temperature Θ_D, Θ_a is based on the assumption that the optical phonon mode in the crystal does not contribute to the lattice thermal conductivity, and only the acoustic mode is taken into account. It can be calculated from the traditional Debye temperature Θ_a[42]

$$\Theta_a = \Theta_D n^{-\frac{1}{3}} \tag{3}$$

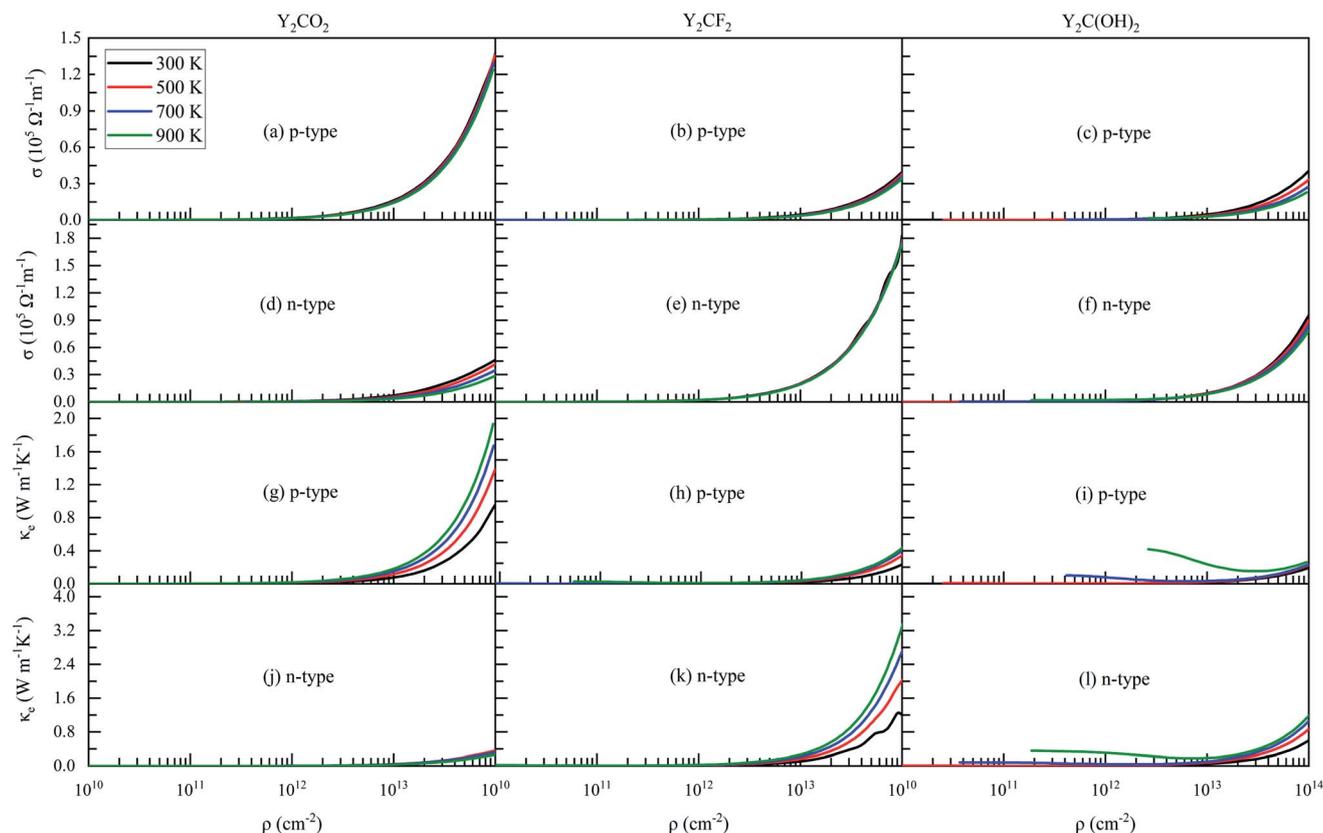where n is the number of atoms in the primitive cell, the thermal conductivity at temperature is estimated by[42]

Fig. 5 Carrier concentration dependence of electrical conductivities (σ) for (a)–(c) p-type and (d)–(f) n-type Y_2CT_2 (T = O, F and OH) and electronic thermal conductivities (κ_e) for (g)–(i) p-type and (j)–(l) n-type Y_2CT_2 (T = O, F and OH).
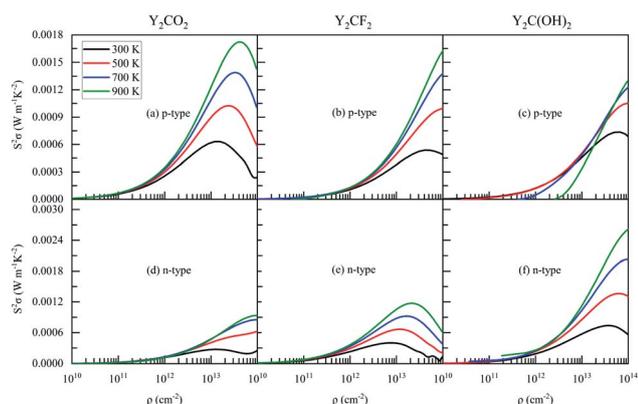

Fig. 6 Carrier concentration dependence of thermoelectric power factors ($S^2\sigma$) for (a)–(c) p-type and (d)–(f) n-type Y_2CT_2 (T = O, F and OH).

$$\kappa_l(T) = \kappa_l(\Theta_D)\frac{\Theta_D}{T} \tag{4}$$

It can be seen from the above formula that the key to calculating κ_l lies in the Grüneisen parameter γ and the acoustic model Debye temperature Θ_a. In this work, we used the elastic constant to calculate the transverse and longitudinal sound velocities, and finally obtain the Grüneisen parameter γ and the

acoustic model Debye temperature Θ_a. The elastic constant, bulk modulus, shear modulus, Young's modulus and Poisson's ratio are shown in Table 3, in which the elastic constant satisfies the Born stability criterion of Born-Huang's lattice dynamics theory of hexagonal two-dimensional structure,[43] *i.e.*, $C_{11} > |C_{12}|$, $(C_{11} + C_{12})C_{33} > 2C_{13}^2$, and $C_{66} > 0$. The transverse sound velocity v_t and longitudinal sound velocity v_l can be calculated *via* the following formulas.[44]

$$v_t = \sqrt{\frac{Y}{2\rho(1+\nu)}} \tag{5}$$

$$v_t = \sqrt{\frac{Y(1-v)}{\rho(1+\nu)(1-2v)}} \tag{6}$$

average sound velocity v_m can be calculated from v_t and v_l,

$v_m = \left[\frac{1}{3}\left(\frac{2}{v_t^3} + \frac{1}{v_l^3}\right)\right]^{-\frac{1}{3}}$, replace v_t, v_l and v_m with expressions for γ and Θ_D:[45,46]

$$\gamma = \frac{9 - 12(v_t/v_l)^2}{2 + 4(v_t/v_l)^2} \tag{7}$$

$$\Theta_D = \frac{h}{k_B}\left(\frac{3n}{4\pi V}\right)^{\frac{1}{3}}v_m \tag{8}$$

Table 3 Y_2CT_2 (T = O, F and OH) average atomic mass m_a, cell volume V, the number of atoms n in the primitive cell, elastic constant C_{ij}, Bulk modulus, Young's modulus, Shear modulus, Poisson's ratio, transverse sound velocity ν_t, longitudinal sound velocity ν_l, average sound velocity ν_m, Debye temperature Θ_D, acoustic Debye temperature Θ_a, Grüneisen parameter γ and lattice thermal conductivity κ_l (at room temperature)

	Y_2CO_2	Y_2CF_2	Y_2CO_2
n	5	5	7
m_a (in amu)	44.36	45.56	31.98
V (Å^3)	288.41	268.19	318.39
C_{11} (GPa)	111.27	81.47	70.30
C_{12} (GPa)	50.48	18.71	15.07
C_{13} (GPa)	1.20	2.05	−2.41
C_{33} (GPa)	2.97	0.87	1.60
C_{66} (GPa)	30.11	30.91	26.45
B (GPa)	19.56	12.12	8.88
Y (GPa)	32.29	19.00	16.44
G (GPa)	13.18	7.67	6.90
ν	0.23	0.24	0.19
ν_t ($\times 10^3$ m s^{-1})	3.21	2.33	2.05
ν_l ($\times 10^3$ m s^{-1})	5.39	3.98	3.31
ν_m ($\times 10^3$ m s^{-1})	3.56	2.59	2.26
Θ_D (K)	274.16	204.17	211.33
Θ_a (K)	160.33	119.40	110.47
γ	1.39	1.45	1.25
κ_l (W m^{-1} K^{-1})	7.16	2.70	2.20

ν_t, ν_l, ν_m, γ and Θ_D are calculated as shown in Table 3. By substituting these parameters into formula (4), the lattice thermal conductivity at room temperature as shown in Table 3 and the κ_l at 300–900 K are shown in Fig. 7. From Fig. 7, for the three compounds, the lattice thermal conductivity decreases with increasing temperature, and the lattice thermal conductivity of Y_2CO_2 is the largest at the same temperature (300–900 K), followed by Y_2CF_2, and $Y_2C(OH)_2$ is the smallest, which means that for the phonon pair of Y_2CO_2 at the same temperature (300–900 K) the thermal conductivity has the largest contribution and $Y_2C(OH)_2$ has the smallest contribution.

Fig. 8 shows the characteristics of the dependence of ZT on carrier concentration. For the n-type carriers, the maximum ZT value at 900 K increases in the order of Y_2CO_2, Y_2CF_2 and $Y_2C(OH)_2$. For the p-type carriers since PF is larger and κ is smaller, the ZT value of Y_2CF_2 is larger than Y_2CO_2 and $Y_2C(OH)_2$. For the Y_2CO_2, PF is larger than Y_2CF_2 and $Y_2C(OH)_2$, but κ is larger than Y_2CF_2 and $Y_2C(OH)_2$, so ZT is smaller than Y_2CF_2 and similar to $Y_2C(OH)_2$.
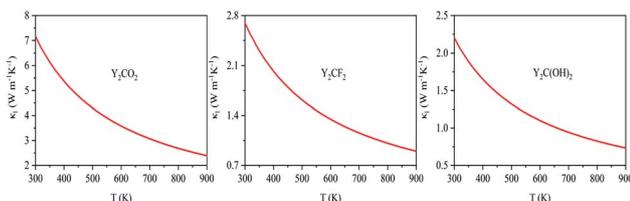
Fig. 7 Lattice thermal conductivity (κ_l) as a function of temperature for Y_2CT_2 (T = O, F and OH).
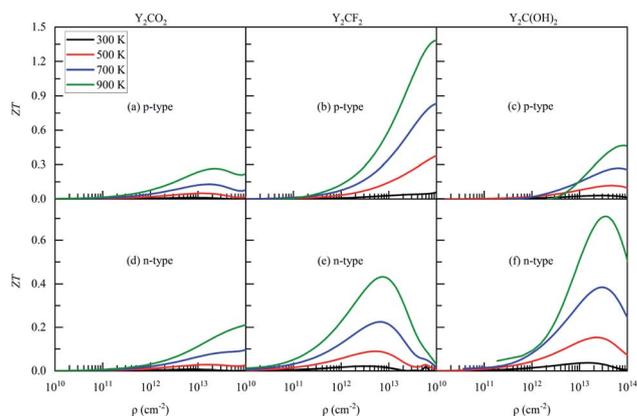

Fig. 8 Carrier concentration dependence of figures of merit (ZT) for (a)–(c) p-type and (d)–(f) n-type Y_2CT_2 (T = O, F and OH).

3.3 Thermodynamic properties

In Fig. 9(a)–(c), we show the volume of Y_2CT_2 (T = O, F and OH) as a function of temperature and pressure. It is found, that under a given pressure, the volume increases with temperature, and this trend decreases with the increase of pressure. On the other hand, at a certain temperature, the volume decreases with the increase of pressure, and this change decreases with increasing pressure, we can understand that the pressure compresses solids and temperature expand solids. The change bulk modulus (B) under temperature and pressure. It can be seen from the Fig. 9(d)–(f) that for the Y_2CO_2, Y_2CF_2 and $Y_2C(OH)_2$, the change of bulk modulus with temperature and pressure is opposite to the change in volume. The bulk modulus of the three functional groups increases with pressure at a given temperature, which means that the pressure increases the hardness. For the Y_2CO_2, Y_2CF_2 and $Y_2C(OH)_2$, the bulk modulus decreases with temperature, which means that the temperature decreases the hardness.

In addition, the heat capacity (C_V) of Y_2CT_2 (T = O, F, OH) is calculated, which provides information about lattice vibration, phase transition, and measurement of molecular motion, and
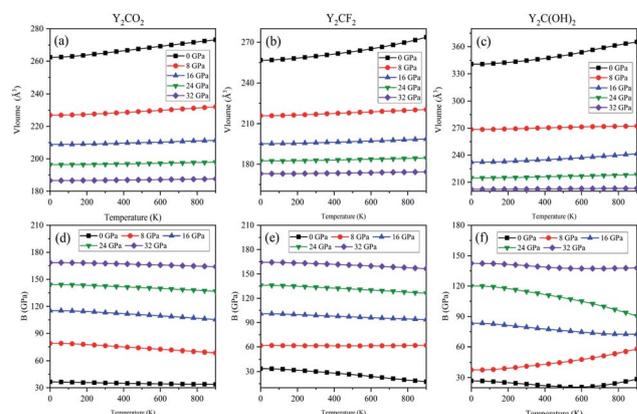
Fig. 9 Temperature dependence of (a)–(c) variations of volume (V) and (d)–(f) bulk modulus (B) for Y_2CT_2 (T = O, F and OH).
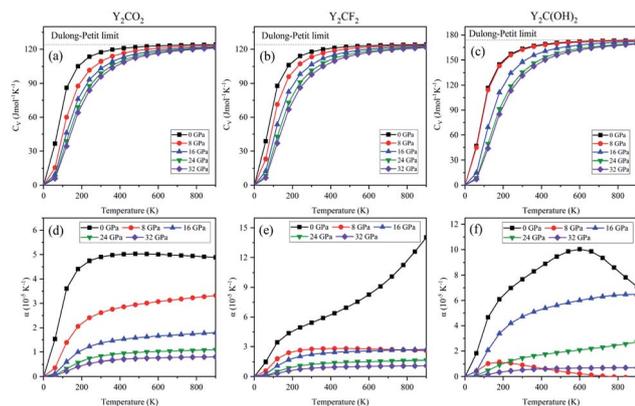
Fig. 10 Temperature dependence of (a)–(c) variations of heat capacity (C_V) and (d)–(f) thermal expansion (α) for Y_2CT_2 (T = O, F and OH).

the changes in it with temperature and pressure are shown in Fig. 10(a)–(c). It can be seen from Fig. 10(a)–(c) that C_V increases rapidly at lower temperature values from 0 K to 400 K. Above 400 K, it can be observed that C_V slowly increases and becomes constant at 700 K, and finally close to the famous Dulong-Petit limit.[47] Thermal expansion is the non-harmonic result of the interatomic force explained by the quasi-harmonic approximation, where it is assumed that the vibration frequency of the network has nothing to do with temperature, but depends on the volume. Fig. 10(d)–(f) shows the change in Y_2CT_2 (T = O, F, OH) thermal expansion α under constant pressure. For low temperatures up to 300 K, α at a given pressure (proportional to T^3) increases sharply with the increase in temperature (most obvious at 0 GPa). Starting from 400 K, the increase becomes gentle. It is obvious that the lower the pressure, the greater the rate of increase. For the three functionalizations, in general, at a given temperature, the thermal expansion decreases with the increase in pressure.

4 Conclusions

We studied the thermoelectric properties of the two-dimensional functionalized Y_2C by considering the transmission of electrons and phonons and studied their electronic structures using first-principles methods, and the Boltzmann transmission equation of electrons was solved. For the transport of phonons, we use the Slack model considering the high-temperature limit to study the contribution of phonons to the thermal conductivity to quantify the study of electrons and lattice pairs. The functional groups O, F and OH opened the band gaps of 2.63 eV, 1.17 eV and 0.74 eV at the Fermi level of Y_2C, respectively. The effective masses of p-type and n-type carriers were calculated through the band structure, thus confirming the difference in the Seebeck coefficient. For the p-type carriers, when the carrier concentration was 4.067×10^{13} cm^{-2}, the maximum power factor of Y_2CO_2 could reach 0.0017 W m^{-1} K^{-2} at 900 K, and at the same temperature, for the n-type carriers, the concentration was 9.376×10^{13} cm^{-2}, the power factor in $Y_2C(OH)_2$ was 0.0026 W m^{-1} K^{-2}. Through the study of

electronic thermal conductivity and lattice thermal conductivity, it was found that the contribution of phonons to thermal conductivity occupies the main part. In particular, the quality factor of Y_2CF_2 was 1.38 at 900 K, because of its low thermal conductivity, indicating that it can be considered as a potential medium-temperature thermoelectric material. In addition, the thermodynamic properties in the range of 32 GPa and 900 K, such as bulk modulus, heat capacity, and thermal expansion, are also estimated using the quasi-harmonic Debye model. Our results may provide some valuable hints for the potential application of Y_2CT_2 (T = O, F, OH) in thermal electric fields. At present, the experimental research on the thermoelectric properties of MXenes materials is still in the research stage, this paper provides a good theoretical basis for experimental research.

Conflicts of interest

There are no conflicts to declare.

Acknowledgements

References

1 X. Shi and L. Chen, *Nat. Mater.*, 2016, **15**, 691–692.
2 X.-L. Shi, J. Zou and Z.-G. Chen, *Chem. Rev.*, 2020, **120**, 7399–7515.
3 F. J. DiSalvo, *Science*, 1999, **285**, 703–706.
4 W. Liu, X. Yan, G. Chen and Z. Ren, *Nano Energy*, 2012, **1**, 42–56.
5 A. Minnich, M. S. Dresselhaus, Z. Ren and G. Chen, *Energy Environ. Sci.*, 2009, **2**, 466–479.
6 P. Qiu, X. Shi and L. Chen, *Energy Storage Mater.*, 2016, **3**, 85–97.
7 A. M. Dehkordi, M. Zebarjadi, J. He and T. M. Tritt, *Mater. Sci. Eng., R*, 2015, **97**, 1–22.
8 R. Moshwan, L. Yang, J. Zou and Z.-G. Chen, *Adv. Funct. Mater.*, 2017, **27**, 1703278.
9 X. Zhang and L.-D. Zhao, *J. Materiomics*, 2015, **1**, 92–105.
10 S. Twaha, J. Zhu, Y. Yan and B. Li, *Renewable Sustainable Energy Rev.*, 2016, **65**, 698–726.
11 T. M. Tritt, *Science*, 1999, **283**, 804–805.
12 F. J. DiSalvo, *Science*, 1999, **285**, 703–706.
13 L. Hicks and M. Dresselhaus, *MRS Online Proc. Libr.*, 1993, **326**, 413–418.
14 L. D. Hicks and M. S. Dresselhaus, *Phys. Rev. B: Condens. Matter Mater. Phys.*, 1993, **47**, 12727.
15 L.-D. Zhao, S.-H. Lo, Y. Zhang, H. Sun, G. Tan, C. Uher, C. Wolverton, V. P. Dravid and M. G. Kanatzidis, *Nature*, 2014, **508**, 373–377.
16 Y. Zhou and L.-D. Zhao, *Adv. Mater.*, 2017, **29**, 1702676.
17 G. Yury and B. Anasori, *Acs Nano*, 2019, **13**, 8491–8494.

© 2022 The Author(s). Published by the Royal Society of Chemistry

18 M. Naguib, M. Kurtoglu, V. Presser, J. Lu, J. Niu, M. Heon, L. Hultman, Y. Gogotsi and M. W. Barsoum, *Adv. Mater.*, 2011, **23**, 4248–4253.

19 Z. Sun, *Int. Mater. Rev.*, 2011, **56**, 143–166.

20 A. Sinha, H. Zhao, Y. Huang, X. Lu, J. Chen, R. Jain, *et al.*, *TrAC, Trends Anal. Chem.*, 2018, **105**, 424–435.

21 S. Kumar and U. Schwingenschlögl, *Phys. Rev. B*, 2016, **94**, 035405.

22 A. N. Gandi, H. N. Alshareef and U. Schwingenschlögl, *Chem. Mater.*, 2016, **28**, 1647–1652.

23 M. Khazaei, A. Ranjbar, M. Arai, T. Sasaki and S. Yunoki, *J. Mater. Chem. C*, 2017, **5**, 2488–2503.

24 L. Hong, R. F. Klie and S. Öğüt, *Phys. Rev. B*, 2016, **93**, 115412.

25 P. E. Blöchl, O. Jepsen and O. K. Andersen, *Phys. Rev. B: Condens. Matter Mater. Phys.*, 1994, **49**, 16223.

26 G. Kresse and J. Furthmüller, *Phys. Rev. B: Condens. Matter Mater. Phys.*, 1996, **54**, 11169.

27 K. B. John, P. Perdew and M. Ernzerhof, *Phys. Rev. Lett.*, 1997, **77**, 1396.

28 P. Blaha, *WIEN2k, An Augmented Plane Wave+ Local Orbitals Program for Calculating Crystal Properties*, ed. K. Schwarz, Techn. Universität Wien, Austria, 2001.

29 M. Khazaei, M. Arai, T. Sasaki, M. Estili and Y. Sakka, *Phys. Chem. Chem. Phys.*, 2014, **16**, 7841–7849.

30 P. B. Allen, W. E. Pickett and H. Krakauer, *Phys. Rev. B: Condens. Matter Mater. Phys.*, 1988, **37**, 7482.

31 W. W. Schulz, P. B. Allen and N. Trivedi, *Phys. Rev. B: Condens. Matter Mater. Phys.*, 1992, **45**, 10886.

32 L. Chaput, P. Pécheur, J. Tobola and H. Scherrer, *Phys. Rev. B: Condens. Matter Mater. Phys.*, 2005, **72**, 085126.

33 G. K. Madsen and D. J. Singh, *Comput. Phys. Commun.*, 2006, **175**, 67–71.

34 G. Mahan and J. Sofo, *Proc. Natl. Acad. Sci.*, 1996, **93**, 7436–7439.

35 G. J. Snyder and E. S. Toberer, *Materials for sustainable energy: a collection of peer-reviewed research and review articles from* Nature Publishing Group, 2011, pp. 101–110.

36 D. A. Broido, M. Malorny, G. Birner, N. Mingo and D. Stewart, *Appl. Phys. Lett.*, 2007, **91**, 231922.

37 W. Li, N. Mingo, L. Lindsay, D. A. Broido, D. A. Stewart and N. A. Katcho, *Phys. Rev. B: Condens. Matter Mater. Phys.*, 2012, **85**, 195436.

38 G. Deinzer, G. Birner and D. Strauch, *Phys. Rev. B: Condens. Matter Mater. Phys.*, 2003, **67**, 144304.

39 A. Ward, D. Broido, D. A. Stewart and G. Deinzer, *Phys. Rev. B*, 2009, **80**, 125203.

40 A. Ward and D. Broido, *Phys. Rev. B: Condens. Matter Mater. Phys.*, 2010, **81**, 085205.

41 Q. Zhang, F. Cao, K. Lukas, *et al.*, *J. Am. Chem. Soc.*, 2012, **134**, 17731–17738.

42 R. Bruls, H. Hintzen and R. Metselaar, *J. Appl. Phys.*, 2005, **98**, 126101.

43 I. Waller, *Acta Crystallogr.*, 1956, **9**, 837–838.

44 O. L. Anderson, *J. Phys. Chem. Solids*, 1963, **24**, 909–917.

45 O. Anderson, *J. Phys. Chem. Solids*, 1959, **12**, 41–52.

46 D. Sanditov, A. Mashanov and M. Darmaev, *Tech. Phys.*, 2009, **54**, 1398–1401.

47 A. Petit and P. Dulong, *Ann. Chim. Phys.*, 1981, **10**, 395.